International Journal of Biological Macromolecules 318 (2025) 145263

Contents lists available at ScienceDirect

International Journal of Biological Macromolecules

journal homepage: www.elsevier.com/locate/ijbiomac

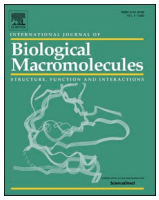

Cellular modulation of a G-quadruplex structure found in the lung cancer-related microRNA-3196

Daniela Alexandre [a,b], Joana Polido [a], André Miranda [a], Robert H.E. Hudson [c], David Monchaud [d], Pedro V. Baptista [b,e,**], Carla Cruz [a,f,*]

[a] RISE-Health, Department of Chemistry, Faculty of Sciences, University of Beira Interior, Rua Marquês d'Ávila e Bolama, 6201-001 Covilhã, Portugal
[b] UCIBIO, Department of Life Sciences, Faculdade de Ciências e Tecnologia, Universidade NOVA de Lisboa, 2829-516 Caparica, Portugal
[c] Department of Chemistry, The University of Western Ontario, London, Ontario, Canada N6A 5B7
[d] Institut de Chimie Moléculaire, ICMUB CNRS UMR 6302, Université Bourgogne Europe (UBE) Dijon, France
[e] i4HB, Associate Laboratory – Institute for Health and Bioeconomy, FCT-NOVA, Portugal
[f] Department of Chemistry, University of Beira Interior, Rua Marquês d'Ávila e Bolama, 6201-001 Covilhã, Portugal

ARTICLE INFO

Keywords:
G-quadruplex microRNA-3196
PhpC ligand
In vitro assays

ABSTRACT

RNA G-quadruplexes (G4s) are promising drug targets due to their high cellular abundance. G-rich RNA regions inherently form G4 structures, while GC-rich sequences adopt stem-loop conformations, and their dynamic equilibrium critically influences RNA function. MicroRNAs (miRs), key regulators of protein expression, undergo processing by Dicer, which specifically recognizes stem-loop structures in precursor miRs (pre-miRs). Notably, some pre-miRs containing G4-forming sequences influence Dicer cleavage, suggesting that G4s can directly regulate miR production. Moreover, pre-miRs with G4 structures present promising targets for small molecules. This research focuses on identifying and modulating G4 structure in pre-miR-3196 to restore normal lung cancer (LC) levels, offering a potential therapeutic strategy. Firstly, bioinformatic analyses indicated the presence of G4 motifs in pre-miR-3196. We then demonstrated *in vitro* that this RNA sequence folds into stable G4s by a combination of biophysical and biochemical assays. Then, we demonstrated the formation of these G4s in human cancer cells by confocal imaging before showing that these G4s can be modulated using the RNA G4 destabilizer PhpC, which impacts the miR-3196 biogenesis. These findings highlighted the possibility of using G4s to control the expression of mature miR-3196 and revealed the potential of using the destabilizer PhpC to adjust its G4 structure.

1. Introduction

DNA and RNA G-quadruplexes (G4s) are secondary structures found in guanine (G)-rich sequences of our genome and transcriptome. These 3D nucleic acid structures consist of stacked G-quartets, which are square planar arrangements of four Gs held together by Hoogsteen hydrogen bonds [1]. G4s are highly stable but also dynamic and polymorphic, their topology being influenced by both internal (sequence, strand stoichiometry, polarity) [2] and external factors (temperature, pH, and cationic content of the buffers) [3]. Given their abundance, localization in key functional regions, and conservation throughout the evolution, G4s are currently being studied for the roles they might play in genetic regulations [1,4,5].

The functions of RNA are reliant on their secondary structures and it is unsurprising that G4s are prevalent in RNA and play key functional roles in both coding and non-coding RNA [6–9]. Efforts have been invested to understand the interplay between G4s and other structures such as hairpins. The modulation of G4s might be strategically exploitable since numerous RNA G4s are implicated in dysregulations underlying genetic diseases, chief among them cancers. Gaining control over their structural plasticity might thus open interesting avenues for treating cancers and, in this line, the use of G4-interacting small

* Correspondence to: Carla Cruz, RISE-Health, Department of Chemistry, Faculty of Sciences, University of Beira Interior, Rua Marquês d'Ávila e Bolama, 6201-001 Covilhã, Portugal.
** Correspondence to: Pedro V. Baptista, UCIBIO, Department of Life Sciences, Faculdade de Ciências e Tecnologia, Universidade NOVA de Lisboa, 2829-516 Caparica, Portugal.
E-mail addresses: pmvb@fct.unl.pt (P.V. Baptista), carlacruz@fcsaude.ubi.pt (C. Cruz).

https://doi.org/10.1016/j.ijbiomac.2025.145263
Received 18 April 2025; Received in revised form 8 June 2025; Accepted 13 June 2025
Available online 15 June 2025

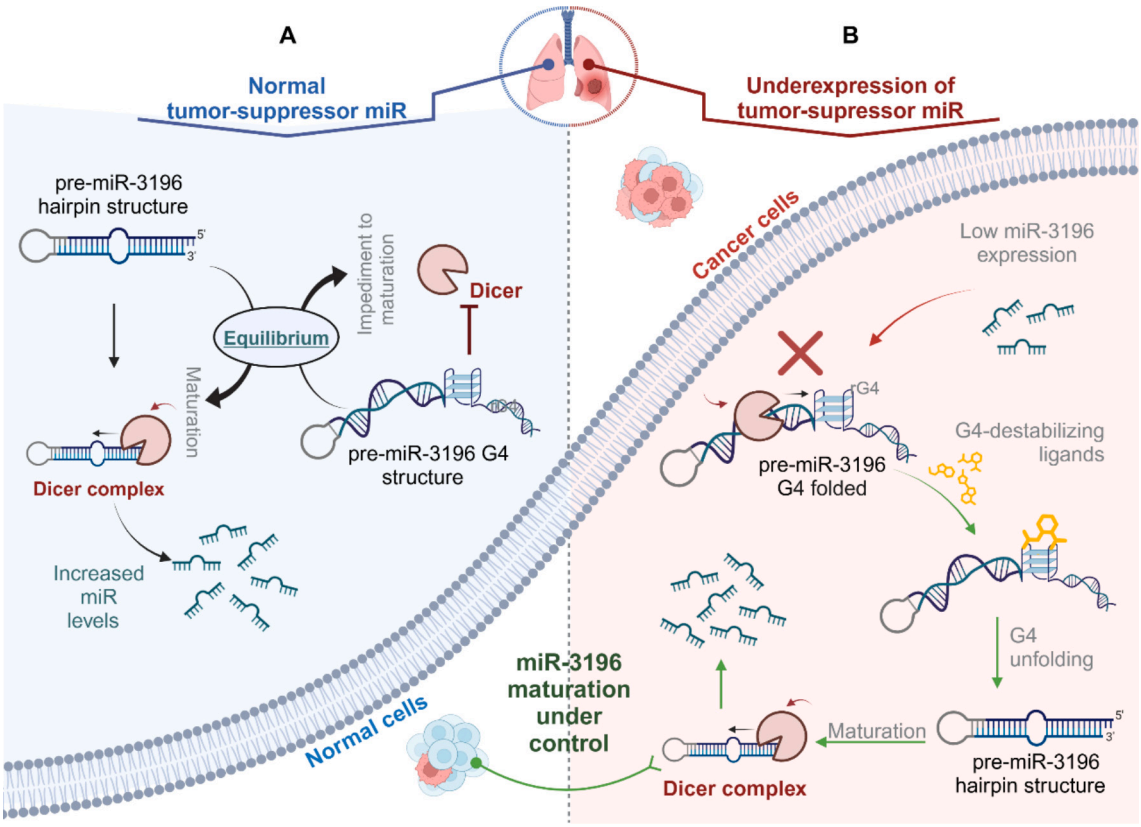

Fig. 1. Schematic representation of the role of the G4 structure in pre-miR-3196 in regulating the expression of mature miR-3196 inside cells. Created with BioRender.

molecules might be strategically relevant [10,11].

While hundreds of DNA G4-interacting molecules (or ligands) have been studied for their ability to take control over DNA G4-associated genomic events (telomere homeostasis, gene expression, *etc.*), far less effort has been devoted to controlling RNA functions [12–14]. Among the possible RNA G4 targets, those belonging to microRNAs (miRs) could yield real therapeutic dividends: miRs are indeed a group of small non-coding RNAs crucial for regulating cellular pathways [15]. Their fine regulation is criticial, as demonstrated by the numerous diseases whose molecular basis originates in miR dysregulation [16].

From a functional point of view, miRs are transcribed by RNA polymerase-II (RNA PolII) and matured in three steps (Fig. 1): i) transcription into primary miR (pri-miR); ii) cleavage by the enzyme Drosha to form a 70 to 80 nucleotide (nt)-long precursor miR (pre-miR); and iii) cleavage by the enzyme Dicer to produce a 20 to 24-nt long mature miR [17]. The mature miR subsequently binds to its specific messenger RNA (mRNA) target, leading to either translation inhibition or mRNA degradation, thus resulting in post-transcriptional repression [18].

From a structural point of view, pre-miRs are known to be G4-prone, with *ca.* 13–16 % of pre-miRs having at least one G4-forming sequence [19]. G4 formation might compete with stem-loop structures, which could in turn affect Dicer processing, potentially reducing mature miR levels in cells [20,21]. Multiple reports have demonstrated that G4s could indeed regulate miR biogenesis, and that their stabilization playing on external factors such as cellular stress, oxidative conditions, metal ions (particularly potassium), and the presence of G4-binding proteins or small molecules, suppresses oncogenic miR maturation and tumorigenesis [22–25]. To go a step further, it could be strategically relevant to use G4-interacting small molecules [26,27]; however, given that it is now accepted that G4 ligands are yet active anticancer agents but can also trigger genetic instability in central nervous system (CNS) cells [28,29], we opted here for the use of molecules able to destabilize G4s, or G4 molecular helicases. Only a few molecular helicases have been reported to date [30], and only a G-clamp analog known as PhpC [31] was studied for its ability to modulate RNA G4s at a transcriptome-wide scale [59].

Herein, we focused on miR-3196, a critical tumor suppressor miR, whose expression is reduced in lung cancer (LC) [32]. Like other miRs, it regulates gene expression post-transcriptionally and negatively affects oncogenic pathways, including SOX12, FOXP4, and PUMA [33–35]. We thus hypothesized that a G4 structure within pre-miR-3196 might negatively regulate its expression in LC, and consequently, that restoring miR-3196 expression could provide new therapeutic avenues for LC. To test this hypothesis, we report herein on i) the *in silico* identification of G4-prone sequence in pre-miR-3196; ii) the *in vitro* confirmation of their ability to fold into G4 structures; iii) the formation of these G4s in LC cells; and iv) the modulation of the G4 landscape using PhpC by both optical imaging and PCR experiments. Our results thus describe a novel strategy for treating cancers according to a brand new and fully innovative approach.

2. Materials and methods

2.1. Oligonucleotide and reagents

All oligonucleotides used (**Table S1**) were acquired from Eurogentec (Liège, Belgium) with HPLC-grade purification, diluted in diethyl pyrocarbonate (DEPC)-treated water at 100 μM for stock solutions, and stored at −20 °C. The concentrations of samples were checked recording the absorbance at 260 nm using TM201 UV–Vis spectrophotometer (Thermo Scientific™; MA, USA) and the molar extinction coefficient (ε) provided by the manufacturer. Before each experiment, the oligonucleotide samples were annealed by heating for 5 min at 95 °C, followed by a fast cooldown of 5 min on ice.

The G4 ligands such as PhenDC3, Thioflavin T (ThT), *N*-methyl mesoporphyrin IX (NMM), and QUMA-1 were obtained from Sigma-Aldrich (St. Louis, MO, USA), and the stock solutions of 10 mM were prepared in Dimethyl sulfoxide (DMSO; Thermo Fisher Scientific™; MA, USA). Further dilutions were carried out using suitable buffers prepared in ultrapure-grade water from a Mili-Q system of Millipore (Burlington, MA, USA). The PhpC ligand was solubilized in 20 mM in DEPC-treated water. The Hoechst 33342® was obtained from Invitrogen™ (H3570; Thermo Fisher Scientific™; MA, USA). All probes were summarized in **Table S2.**

The biophysical experiments were conducted in potassium-containing buffers with controlled ionic strength. The buffers included 10 mM lithium cacodylate (LiCaco; pH 7.2) with varying concentrations of potassium and/or lithium chloride to create K1 (1 mM KCl, 99 mM LiCl), K10 (10 mM KCl, 90 mM LiCl), K20 (20 mM KCl, 80 mM LiCl), and K100 (100 mM KCl). Also, to mimic the intracellular environment *in vitro*, a stock solution with KCl (150 mM K^+), NaCl (10 mM Na^+), $MgCl_2$ (1 mM Mg^{2+}), $CaCl_2$ (0.0001 mM Ca^{2+}), $NaHCO_3$ (10 mM HCO_3^-), HEPES (15 mM), glucose (5 mM), NaH_2PO_4 (30 mM) and BSA (0.5 mg/mL), called intracellular mimic buffer (IMB), were prepared. The phosphate-buffered saline (PBS) Dulbecco's Formula DPBS 10× was purchased from bioWORLD (Dublin, USA). Deuterium oxide (D_2O) acquired from Merck Millipore (CAS: 7789-20-0; USA) was used for NMR sample preparation. For electrophoresis experiments, the TBE buffer was made from 89 mM Tris-base (Fisher Scientific, USA), 89 mM boric acid (ChemLAB, Belgium), and 1 mM EDTA (PanReac, Spain), and the acrylamide/bisacrylamide 40 % reagent is obtained from GRISP (ref. GB16.4037; Porto, Portugal).

The adenocarcinoma human alveolar basal epithelial (A549 - ATCC CCL-185) cell line was obtained from ATCC (USA). The Nutrient mixture F-12 Ham (Hams-F12) was purchased from Sigma-Aldrich (ref. N3520; ST. Louis, MO, USA) and reduced-serum medium Opti-MEM from Gibco (ref. 22600–134; Thermo Fisher Scientific™; MA, USA). Lipofectamine RNAiMax transfection reagent was used and purchased from Invitrogen (ref. 13778150; USA) for sequence transfection.

2.2. Bioinformatic analysis

The G4 propensity of the hsa pre-miR-3196 sequence was evaluated through a bioinformatics approach. First, the sequence was obtained from the miRbase database (https://www.mirbase.org; [36]), and its most likely secondary structure was predicted using the RNAstructure software (https://rna.urmc.rochester.edu/RNAstructureWeb/; [37]). The potential regions forming G4s (rG4) were then identified using the QGRS-mapper algorithm (https://bioinformatics.ramapo.edu/QGRS/analyze.php), with default parameters set to a maximum length of 30 nucleotides (nt), a minimum G-group size of 2, and a loop size range of 0 to 36 nucleotides. Additionally, the sequences were analyzed using the G4 Hunter v.2.0 Web tool (https://bioinformatics.cruk.cam.ac.uk/G4Hunter/; [38]), applying a window size of 25 nucleotides and a threshold score of ≥1.2, which balances minimizing false positives and false negatives.

2.3. Circular dichroism spectroscopy

The Jasco J-815 spectrometer (Jasco, USA), equipped with a multi-holder and a Peltier-type temperature controller (model CDF-426S/15), was used for CD acquisitions. The spectra were obtained on high-precision quartz cuvettes (ref. 115B-10-40; Hellma Analytics, Germany) at 37 °C in a wavelength range between 220 and 320 nm, at a scanning speed of 100 nm/min with a 0.5 nm bandwidth, 0.5 s integration time, and over 3 accumulations. The sample concentration was adjusted to achieve an absorbance close to 0.8, following the Lambert-Beer law and accounting for the molar extinction coefficient (ε), and annealed in potassium-containing buffers or IMB as previously specified. The data was then smoothed and converted to molar dichroic absorption (Δε) using Eq. (1).

$$\Delta\varepsilon = \frac{\theta}{32980 \times c \times l} \tag{1}$$

where θ is ellipticity in millidegrees, c is the oligonucleotide concentration (mol L^{-1}), and l is the path of the length in cm. In addition, the conformation index r was calculated following Eq. (2), as reported by Chen et al. [39]:

$$r = \frac{CD_{265}}{|CD_{265}| + CD_{290}} \tag{2}$$

where CD_{265} and CD_{290} are the molar dichroic absorption of peaks. Parallel, hybrid, and antiparallel conformation have $1 > r \geq 0.5$, $0.5 > r > 0$, and $r < 0$, respectively.

In the CD melting experiments, the spectra were recorded at the wavelength of the maximum absorbance (240 nm), while the samples were heated from 25 °C -95 °C at a rate of 1 °C/min. The acquired data were analyzed and converted into folded fractions, according to Eq. (3), when the ellipticity at each temperature is represented by CD, while CD_λ^{max} and CD_λ^{min} are the maximum and minimum ellipticity values obtained.

$$f = \frac{CD - CD_\lambda^{min}}{CD_\lambda^{max} - CD_\lambda^{min}} \tag{3}$$

when the ellipticity at each temperature is represented by CD, while CD_λ^{max} and CD_λ^{min} are the maximum and minimum ellipticity values obtained. To determine the melting temperature (T_m) value (°C), *i.e.*, the temperature for which the normalized emission is 0.5, the resulting graph was fitted to a Boltzmann distribution equation using the OriginPro2021 software (OriginLab, MA, USA).

2.4. UV–vis spectroscopy

All UV–Vis experiments were conducted using a TM201 UV–Vis spectrophotometer (Thermo Scientific™; MA, USA). Spectra were measured in high-precision quartz cuvettes (ref. 115B-QS; Hellma Analytics, Germany) between 220 and 340 nm wavelengths at a scanning rate of 300 nm/min 0.5 nm data intervals, 0.05 s integration time, and automatic baseline correction. Oligonucleotides were used at a concentration of 3 μM in all UV–Vis experiments.

For **thermal difference spectra (TDS)**, the rG4–3196 oligonucleotide solution was annealed in K1 buffer, as previously mentioned. Two spectra were acquired, the first recorded at RT (folded state) and the second at 95 °C (unfolded state) after an incubation time of 15 min. TDS represents the arithmetic difference between spectra in folded and unfolded conditions. The resulting spectra were normalized to the maximum absorbance, and TDS factors ΔA240nm/ΔA295nm, ΔA255nm/ΔA295nm, and ΔA275nm/ΔA295nm were calculated [40,41].

For **isothermal difference spectra (IDS)**, the rG4–3196 oligonucleotide solution was annealed in 10 mM LiCaCo buffer (pH 7.2) as described above. A spectrum was first recorded at 25 °C in the absence of potassium (unfolded state), and a second spectrum was taken after adding KCl 1 M to a final concentration of 100 mM, equilibrating for 30 min (folded state). Spectra were adjusted for dilution factor, and IDS represents the difference between the spectra in the folded and unfolded conditions [42]. The resulting graphs were analyzed using the OriginPro2021 software (OriginLab, MA, USA).

2.5. ^{1}H nuclear magnetic resonance (NMR)

^{1}H NMR spectra were recorded using a 600 MHz Bruker Avance III spectrometer (Bruker Corporation, Massachusetts, USA), operating at a ^{1}H Larmor frequency of 600.10 MHz, equipped with an inverse

detection triple-resonance *z*-gradient QCI cryoprobe. We applied the *zgesgp* water suppression pulse sequence using the following parameters: 32 K data points, relaxation delay of 2 s, and 1024 scans for a spectral width of 12.019 Hz centered at the water resonance. The samples were prepared in 3 mm NMR tube, total volume of 180 μL comprising 100 μM of rG4–3196 in 10 mM LiCaCo buffer (pH 7.2) supplemented with 10 % (*v*/v) of D_2O. In the salt titration experiments, increasing amounts of KCl 1 M were directly added into the tube, achieving final concentrations of 0, 1, 10, and 100 mM KCl. Between titration points the sample was annealed as previously described. We also examined the effect of the PhpC ligand on the topology of rG4–3196, analyzing the spectral changes without and with increasing amounts of PhpC (1, 5, 10, 20 M equiv.). Chemical shifts (δ) were measured in ppm, and all spectra were analyzed using Bruker TopSpin4.1 software (Bruker Corporation; MA, USA). Images were prepared using MestReNova (Santiago de Compostela, Spain).

2.6. Native polyacrylamide gel electrophoresis (PAGE)

A native PAGE was carried out with a specific dye (NMM; **Table S2**) to visualize and assess the formation and molecularity of the G4 structure. Firstly, the rG4 sequences (**Table S1**) at a concentration of 6 μM in DEPC-treated water were prepared and heated at 95 °C for 5 min. Afterward, a buffer solution containing 20 mM LiCaco and 200 mM KCl was added. The samples were then annealed as previously described. Sucrose was supplemented to all samples to achieve a final concentration of 15 % sucrose, 10 mM LiCaco, 100 mM KCl, and 3 μM rG4 sequences.

The samples were loaded in a 20 % polyacrylamide gel (19:1), previously pre-runned for 30 min, and then the gel was run at 110 V for 210 min at 4 °C in running buffer (1× TBE). The single-stranded oligothymidylate markers of various lengths (9, 15, 21, 30, 60, and 90 nt) and the samples were loaded, and then the gel was run at 110 V for 210 min at 4 °C in running buffer (1× TBE).

Thereafter, the gel was post-stained with 2.5 μM of NMM for 30 min under agitation to visualize the G4 using a ChemiDoc™ MP Imaging System (Bio-Rad; CA, USA) and with 1× SYBR Gold (Invitrogen, USA) for 20 min to compare with other structures. The rG4–149 sequence was used as a positive control in the assay [43]. Images were prepared using ImageLab (Bio-Rad, CA, USA).

2.7. Size-exclusion chromatography (SEC) assay

The SEC experiments were performed following the reported protocols using an AKTA FPLC (GE Healthcare Life Sciences, USA) with a Superdex 30 Increase 3.2/300 column (3.2 mm × 300 mm composite of cross-linked agarose and dextran, particle size 9 μm, ref. 29,219,758; Cytiva, MA, USA) [44,45]. Before starting the experiments, the column was equilibrated in elution buffer (Tris-HCl 10 mM pH 7 supplemented with 100 mM KCl). Before injection, the rG4–3196 was annealed in elution buffer (final concentration 20 μM), as previously described, and subsequently, 15 μL of the sample was injected and eluted at 0.150 mL/min rate with a column temperature of 20 °C. The elution process was monitored by the absorbance at 260 nm, and then chromatograms were normalized and plotted in OriginPro2021 software software (OriginLab, MA, USA). Additionally, the chromatograms were deconvoluted using a Gaussian model to evaluate the relative amount of each species.

2.8. Fluorescence light-up probe assays

Fluorescence light-up probe assays are commonly used to detect and study G4 sequences. The fluorescence intensity of probes was measured using a GloMax® Explorer Multimode Microplate Reader (Promega, USA). The ThT and NMM were excited at 420 nm and 380 nm wavelengths, with their respective fluorescence emissions recorded at 490 nm and 610 nm. Before measurements, the plate was agitated for 5 min and then incubated at RT for 10 min. Each well contained 52 μL of K100 buffer, 40 μL of oligonucleotide (final concentration of 3 μM), and 8 μL of probe (final concentration of 2 μM). Three independent experiments were conducted, using positive (26CEB and rG4–149 sequences) and negative (ds26 sequence) controls. The resulting graphs were analyzed using the OriginPro2021 software (OriginLab, MA, USA). All experimental groups were measured in triplicate.

2.9. Förster resonance energy transfer (FRET) experiments

2.9.1. FRET-melting competition (FRET-MC)

The FRET-MC assay was carried out as described by J-L Mergny et al. [46]. Experiments were performed in 96-well plates using a CFX Connect™ Real-Time PCR instrument (Bio-Rad, CA, USA) equipped with FAM filters ($\lambda_{ex} = 492$ nm; $\lambda_{em} = 516$ nm) in a working volume of 25 μL per well. The sequence (F21T and rG4–3196) and ligand solutions (PhenDC3) were prepared in K10 buffer, and each condition was tested across three different plates. Each well contained 0.2 μM of the F21T fluorescent oligonucleotide, either with or without 0.4 μM of the G4 ligand (PhenDC3) and 3 μM of competitor (rG4–3196 sequence). The equipment was set to record FAM emission while increasing the temperature stepwise by 0.5 °C every 60 s, from 25 °C to 95 °C. The FAM emission was normalized (0 to 1) and fitted using a Boltzmann model in OriginPro2021 software (OriginLab, MA, USA) to determine the T_m (the temperature for which the normalized emission is 0.5). The ΔT_m values (°C) were calculated by the difference in Tm of F21T in the presence and absence of competitor and PhenDC3 ligand. To assess and quantify the competitive effects of the competitors, the S Factor was calculated according to Eq. (4).

$$\text{S factor} = \frac{\Delta T_m\ (\text{F21T} + \text{Competitor})}{\Delta T_m\ (\text{F21T})} \tag{4}$$

Effective competitors yield an S factor value near 0, whereas the S factor stays close to 1 for weak or ineffective competitors. The experiments were conducted in triplicate across three separate plates.

2.9.2. Isothermal-FRET (isoFRET)

The isothermal competition experiment was conducted as described previously [47] in non-binding 96-well microplates (ref. 650,901; Greiner Bio-One GmbH; Kremsmünster, Austria). The samples were predenatured and diluted in K20 buffer in this assay. To summarize, we combined 5 μL of competitor (2.5 μM), 5 μL of 37Q (1 μM), and 10 μL of PhenDC3 (2.5 μM) or K20 buffer in no-PhenDC3 conditions. The mixture was then gently mixed and incubated for 5 min. Afterward, 5 μL of F22 (100 nM) was added. Control experiments were also carried out using F22 with and without 37Q, as well as with G4 and non-G4 forming sequences. Before measurement, the plates were incubated at 37 °C for 24 h, and fluorescence signals were recorded using a TECAN Infinite M1000 Pro plate reader (TECAN Salzburg, Austria). The F factor was calculated using the OriginPro2021 software (OriginLab, MA, USA) with Eq. (5), and the fluorescence intensities were plotted. The F factor represents the impact of a competitor on the F22-37Q hybridization in the presence of PhenDC3, based on fluorescence intensities (FI).

$$\text{F factor} = \frac{\text{FI}_{\text{Competitors}} - \text{FI}_{\text{F22+37Q duplex}}}{\text{FI}_{\text{F22}} - \text{FI}_{\text{F22+37Q duplex}}} \tag{5}$$

The experiments were conducted in triplicate, using positive (26CEB and rG4–149 sequences) and negative (ds26 sequence) controls.

2.10. Fluorescence titrations

Fluorescence titration experiments were conducted on a FluoroMax4 spectrofluorometer (Horiba, Japan) in a 10 mm path-length quartz suprasil cuvette (ref. 105.251-QS; Hellma Analytics; Germany) for PhpC ligand interaction studies. The titrations were performed in 50 μL (final

(A)

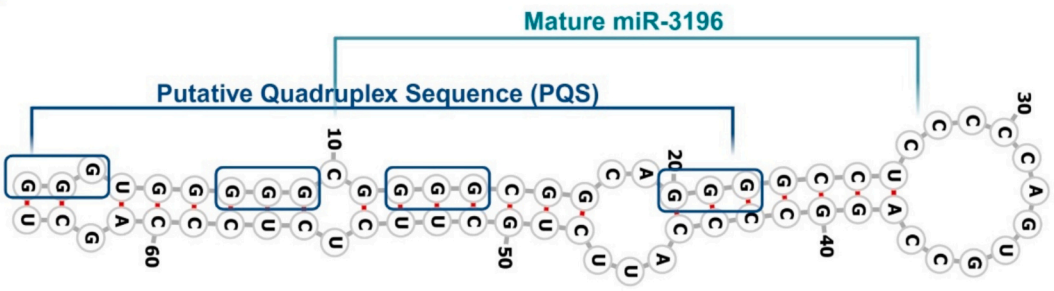

(B)

	Sequence (5´to 3´)	PQS	G-score	
pre-miR-3196	GGGUGGGGCGGGGCGGCAGGGGCCUCCCCCAG UGCCAGGCCCCAUUCUGCUUCUCUCCCAGCU (64nt)	GGGUGGGGCGGG GCGGCAGGG (22nt)	QGRS-mapper 39	G4 Hunter 2.7

Fig. 2. (A) Predicted hairpin structure of the pre-miR-3196 by the RNA structure software. The box-defined areas highlight the G-tracts involved in the G4 folding. **(B)** Pre-miR sequence and the PQS with respective G-scores.

volume) by adding successive molar equivalents (25 to 5000 nM, 0.25 to 50 mol. equiv.) of PhpC ligand to pre-annealed rG4–3196 sequence (100 nM in IMB buffer), followed by 3 min of equilibration time between each titration point. All fluorescence spectra were scanned with an excitation wavelength of 495 nm, an emission wavelength range of 510–700 nm, and excitation and emission slits of 2 nm. The measurements were taken at 37 °C, and the average of three scans was calculated. The resulting fluorescence data were converted into bound RNA fraction (α) plots using Eq. (6):

$$\alpha = \frac{I - I_{\lambda}^{free}}{I_{\lambda}^{bound} - I_{\lambda}^{free}} \quad (6)$$

where I represent the fluorescence intensity at 523 nm for ligand: rG4 ratio and I^{free} and I^{bound} are the fluorescence intensities of the free and bound ligand, respectively. Additionally, a Michaelis-Menten saturation binding model was applied to fit the data points using OriginPro2018 software (OriginLab, MA, USA) based on Eq. (7):

$$v = \frac{V_{max} \times [Ligand]}{K_D + [Ligand]} \quad (7)$$

where K_D is the Michaelis constant, describing the ligand concentration at which the reaction rate is half of V_{max}, and [Ligand] is the concentration of the ligand. Three independent experiments were used.

2.11. Cellular experiments

For cellular studies, the A549 cell line was routinely cultured in 75 cm^2 tissue culture flasks at 37 °C in a humidified 5 % CO_2 atmosphere in Hams-F12 medium supplemented with 10 % (v/v) fetal bovine serum and 1 % (v/v) Penicillin-Streptomycin.

2.11.1. Live cell imaging

For confocal fluorescence microscopy experiments with live cells, after trypsinization, the cells were plated in 8-well μ-slides (IBIDI; GmbH, Germany) at a density of 5×10^3 cells *per* well and allowed to adhere for 24 h at 37 °C with 5 % CO_2. Afterward, 50 nM of FAM-rG4–3196 sequence was transfected using RNAiMAX Lipofectamine according to manufacturer instructions for 24 h at 37 °C. Subsequently, cells were washed once with fresh Opti-MEM, incubated with 0.25 μM fluorescent RNA G4 probe QUMA-1 for 15 min, and then with Hoechst 33342 nuclear dye (2 μM) for 10 min.

To test the effect of PhpC, after transfection of the FAM-rG4–3196 sequence, the cells were washed once with fresh Opti-MEM and incubated with different concentrations of PhpC ligand (50 and 100 μM) for 24 h at 37 °C. After that, the cells were stained with Hoechst 33342 and a QUMA-1 probe, as mentioned above.

After all incubation periods, the cells were visualized using a Zeiss AxioObserver LSM 710 confocal laser scanning microscope (Zeiss, Germany) coupled with a plane-apochromat 63×/DIC objective, and the obtained images were adjusted in Zeiss Zen Software (Zeiss, Germany). Fluorescence images were taken at 63× magnification, and two independent experiments were conducted using all control conditions. Finally, the ImageJ software (USA) was used to determine colocalization coefficients and the mean fluorescence intensity.

2.11.2. miRs expression

To test the effect of PhpC ligand in the endogenous level of the mature miRs, the A549 cells were plated in 24-well culture plates at a density of 0.5×10^5 cells *per* well and allowed to adhere for 24 h at 37 °C with 5 % CO_2. Subsequently, the culture medium was replaced by fresh Hams-F12 with different concentrations of ligand (25, 50, and 100 μM) for 24 h. After incubation, the culture medium was removed, and cells were detached with trypsin solution. According to the manufacturer's instructions, total RNA was extracted from cells using miRNeasy Mini Kit (Qiagen, Hilden, Germany). The concentration of RNA extracts, resuspended in DEPC-treated water, was measured spectrophotometrically with a NanoDrop ND1000 (Thermo Fisher Scientific, Waltham, MA, USA) at a wavelength of 260 nm. The Reverse Transcriptase-quantitative Polymerase Chain Reaction (RT-qPCR) reaction was carried out using a miRCURY LNA RT Kit, miRCURY LNA SYBR® Green Kit, and specific primer sequences (Qiagen, Hilden, Germany) and was performed in a CFX Connect™ Real-Time PCR Detection System (Bio-Rad, Hercules, CA, USA). The reaction mixture was prepared according to the manufacturer's instructions in a final volume of 10 μL and conducted at 95 °C for 2 min, followed by a 2-step cycle. This cycle consisted of denaturation at 95 °C for 10 s, followed by annealing and extension at 56 °C for 60 s, then repeated for 40 cycles. The data were analyzed using the comparative threshold cycle (Ct) method, 2 − (ΔCt target − ΔCt control), where relative gene expression levels in each sample are

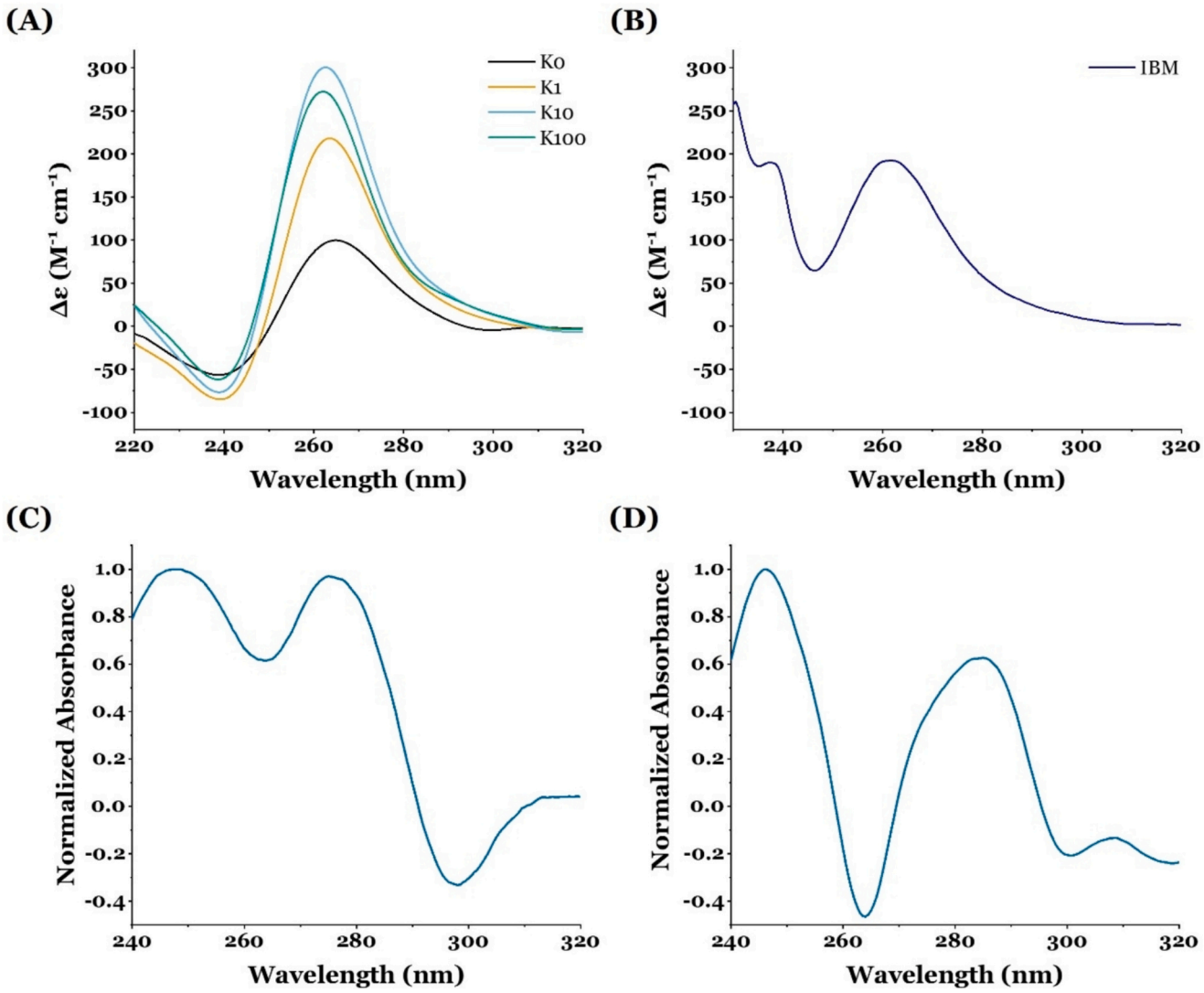

Fig. 3. Circular dichroism spectra of rG4 pre-miR-3196 with increasing amounts of KCl **(A)** and in IMB **(B)** at 37 °C. TDS **(C)** and IDS **(D)** spectra of rG4–3196 sequence. Both spectra were acquired in K1 and K100 buffers, respectively. The spectra were obtained by calculating the arithmetic difference between the spectra in folded and unfolded states.

determined by quantifying the target miRs relative to the endogenous control gene (U6) and normalizing to the control condition. Comparing the effect of PhpC ligand in expression levels of other G4-prone miRs, such as miR-let7e, was also evaluated by RT. At least three independent repeats for each experiment were carried out.

2.12. Statistical analysis

All descriptive data were expressed as the mean ± SD, and GraphPad software (version 8.0.1) was applied for statistical analysis. The Shapiro–Wilk test was performed on all data to test the normality of the distribution. Specifically, the Kruskal-Wallis test with Dunn's multiple comparison test was used to analyze integrated fluorescence. To analyze the results of NMM, ThT and FRET experiments, the one-way ANOVA test with Sidak's multiple comparison test was used. The two-way ANOVA test with Bonferroni's multiple comparisons test was used to compare miR expression levels after PhpC treatment of A549 cells. In addition, the statistical significance was determined based on ρ-values, with a ρ-value <0.05 considered statistically significant.

3. Results and discussion

A subset of pre-miRs was reported to harbor putative G4-forming sequences (PQSs), in which G4s were suspected to modulate Dicer-mediated cleavage, that is, modulate both miR production and function. Herein, we thus first focused on both pre-miR-3196 and mature miR-3196 expression in A549 cells (**Fig. S1**).

3.1. Identification of PQSs in hsa pre-miR-3196

Bioinformatics was undertaken to determine the presence of G4 motifs in the human (*homo sapiens*, hsa) pre-miR-3196 sequence. The sequence was retrieved from miRbase, and G4 motifs were investigated using both QGRS-mapper and G4 Hunter, which provide G-score and G4H score, respectively. In pre-miR-3196, 362 PQS were identified, including a particular sequence that displays both high G-score (39) and G4H score (2.5). This sequence, displayed in Fig. 2, could adopt both G4 and hairpin structures; it is located near the 5′-end of pre-miR, the privileged site of Dicer binding [48], making it an excellent candidate for subsequent studies.

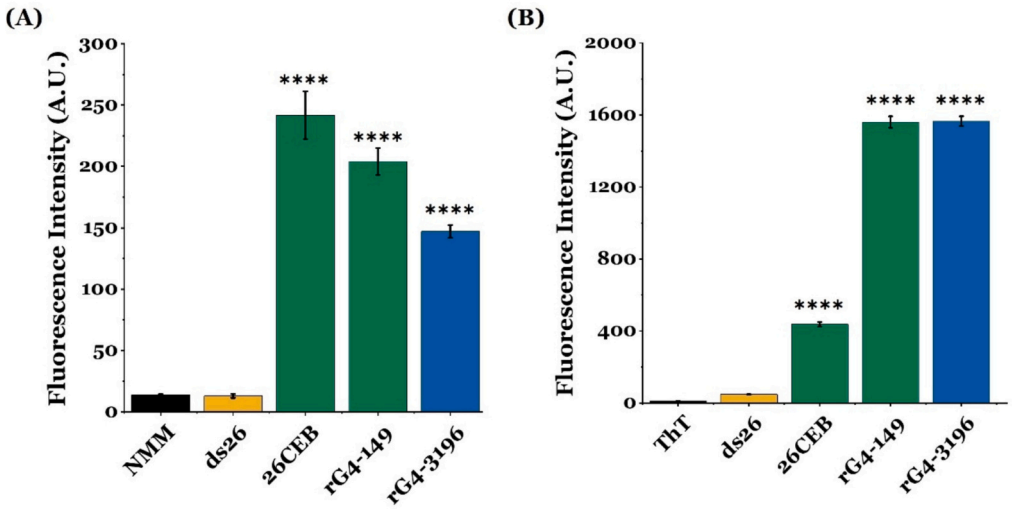

Fig. 4. Light-up fluorescence experiments using **(A)** NMM and **(B)** ThT G4 probes. For both assays, fluorescence increases in the presence of a sequence adopting a G4 fold. Negative controls in orange, positive controls in green, and the tested rG4 sequence in blue. The one-way ANOVA test with Sidak's multiple comparison test correction was used to determine the significance of the correlation compared to NMM and ThT conditions, and values are expressed in mean ± SD and displayed on bars. ****$\rho < 0.0001$.

3.2. *In vitro characterization of hsa pre-miR-3196 G4*

A series of biophysical techniques were implemented to characterize the formation of a G4 structure within the identified pre-miR-3196 sequence. CD spectroscopy was first used with rG4–3196 sequence folded in buffers with an increasing concentration of KCl (from 0 to 100 mM). As seen in Fig. 3(A), typical parallel G4 signatures were observed with a positive peak around 260–265 nm and a negative peak near 240–245 nm, in line with the privileged parallel topology of RNA G4s. Of note, a stable G4 fold was observed at the lowest concentration of KCl (1 mM), highlighting its high stability. Interestingly, the same typical bands of parallel G4 topology were also observed in the IMB (Fig. 3(B)), suggesting the ability of this sequence to form a G4 structure inside cells. These spectral observations were confirmed by CD-melting experiments which indicate that the melting temperatures (T_m, **Fig. S2(A)** and **Table S3**) ranged from 54 °C (in 1 mM KCl) to >72 °C (in 100 mM KCl). During the CD experiments, high tension (HT) voltage values were monitored to confirm data quality for G4 folding characterization. All values remained below critical thresholds (typically <600 V), indicating reliable signal detection. Representative HT spectrum is provided in **Fig. S2(B)**.

We then conducted UV-spectroscopy investigations and more particularly thermal difference spectra (TDS) experiments: due to the high thermal stability observed in CD-melting, the spectra were recorded in 1 mM KCl buffer to ensure unfolding at high temperatures [40]. The spectra seen in Fig. 3(C) (and **Table S4**) indicates the typical parallel G4-specific shape, with two positive peaks at 245 nm and 263 nm along with a negative peak *ca.* 295 nm. In Fig. 3(D), the isothermal difference spectra (IDS) which further exploits the cation-dependent nature of the G4 folding, confirmed the G4 fold of miR-3196 sequence in 100 mM KCl buffer, as indicated by hypochromic at 295 nm and 263 nm and positive band at 245 nm [42].

We next performed NMR investigations, using as above increasing KCl concentrations at 37 °C, to evaluate the effect of K^+ on the G4 fold (analyzing the so-called 'imino' protons involved in Hoogsteen base pairing, at 10–12 ppm) [49,50]. The rather broad spectrum seen in **Fig. S3** (and **Table S5**) yet confirmed the G4 fold of miR-3196 sequence even at the lowest KCl concentration (1 mM) but also indicated an intrinsic polymorphism, which does originate in different G4 topologies (the G4s have been characterized as parallel) but in the existence of multiple G-runs in the sequences, which allows for the formation of different types of G4s [51].

We next evaluated the molecularity of the G4s using non-denaturing polyacrylamide gel electrophoresis (PAGE), performed as above under K^+-rich conditions. After migration, the gel was sequentially post-stained with *N*-methyl mesoporphyrin IX (NMM), a routinely used G4-specific light-up probe, and SYBR Gold, a pan-nucleic acid labelling agent [52]. Results seen in **Fig. S4** confirmed the G4 fold of miR-3196 sequence, as a band migrating as the positive control G4 (miR-149) was seen, but this gel also confirmed a possible mixture of intra-molecular G4s, as a smeared band was observed right below that of G4s. To confirm this, size-exclusion chromatography (SEC) was undertaken (**Fig. S5**): the chromatograms obtained confirmed that the G4 of miR-3196 is mostly an intra-molecular G4 structure (*ca.* 82 %) along with a minor contribution of a dimeric form (18 %). Also, to favor and increase intramolecular folding, the slow cooling down protocol was employed and revealed that can favor the intra-molecular form (86 %, *versus* 14 % of dimeric form).

We then further exploited the G4-specificity of NMM, and also used the other well-known light-up probe ThT for performing fluorescence titrations [53]. As seen in Fig. 4, the two dyes strongly emit upon interaction with miR-3196, in a manner reminiscent of what was observed with two positive controls (26CEB and rG4–149; the duplex ds26 was used herein as a negative control). Altogether, these results demonstrate that the sequence of miR-3196 does fold into a G4 structure.

To go a step further and gain additional insights into the ability of miR-3196 to fold into G4, we performed the FRET-MC assay [54]. This competitive assay relies on the displacement of PhenDC3, a well-known G4 stabilizer [54], from the doubly labeled telomeric G4 F21T by an excess of putative G4 candidate, here miR-3196 [55]. The results seen in Fig. 5(A) demonstrated that an excess (15 mol. equiv.) of miR-3196 displaced PhenDC3 from F21T, its thermal stabilization going from $T_m = 19.5 \pm 0.6$ °C to nearly 0 °C, which thus confirmed the G4 fold of miR-3196. Additionally, we performed the isoFRET method, which is an isothermal (37 °C) competitive assay [47]: here, PhenDC3 is displaced from the mono-labeled G4 37Q, the efficiency of this displacement being quantified upon hybridization of 37Q with the FAM-labeled complementary C-rich sequence F22. The results seen in Fig. 5(B) are consistent with the previous findings, indicating that miR-3196 displaced PhenDC3 from 37Q (quantified by the F Factor which explains that F values below 0.27 are characteristic of a G4 competitor, above 0.54 correspond to

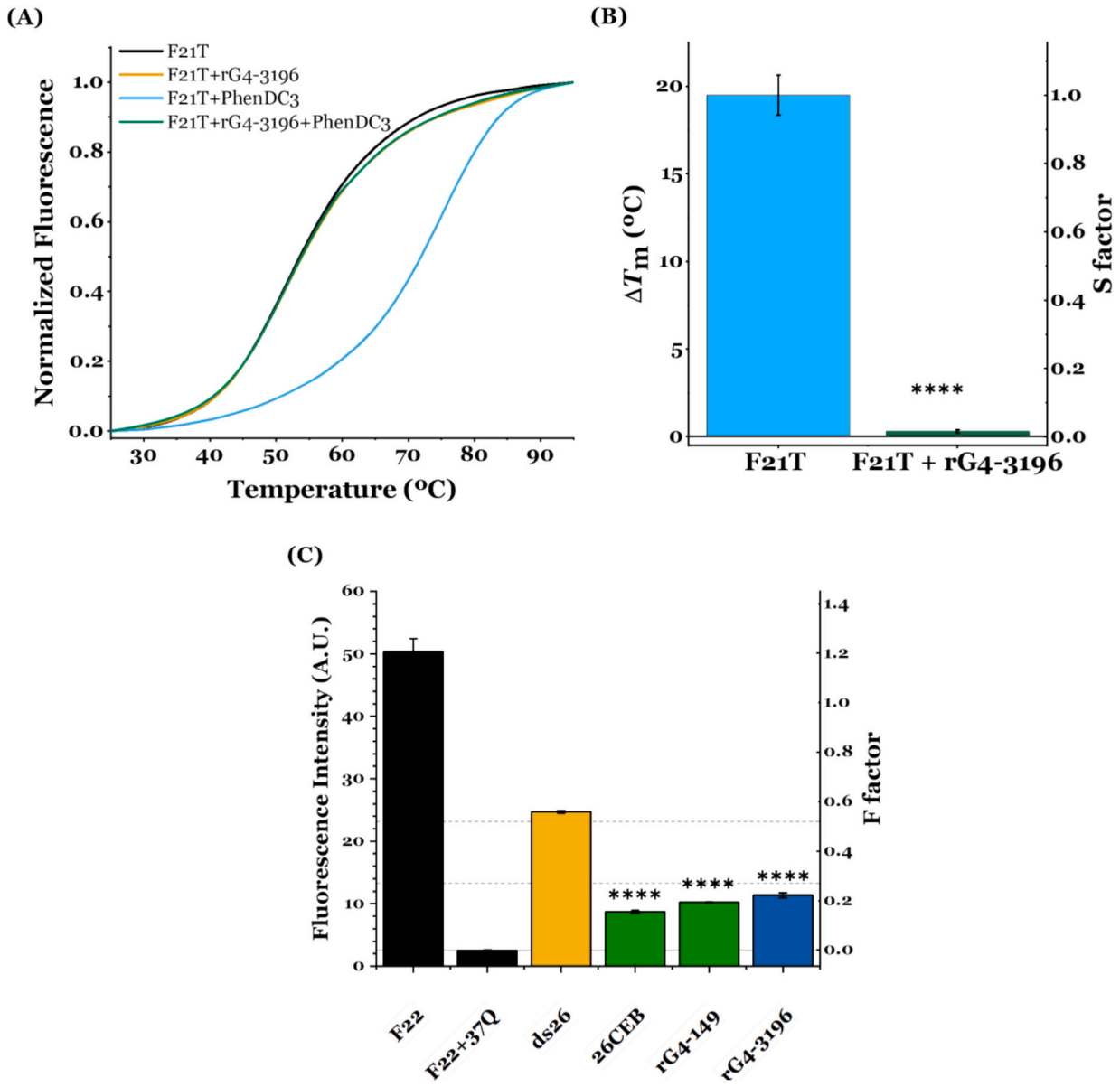

Fig. 5. FRET-MC **(A, B)** and Iso-FRET experiments **(C)** show the formation of G4 in the rG4-3196 sequence. Negative controls in orange, positive controls in green, and the tested rG4 sequence in blue. The one-way ANOVA test with Sidak's multiple comparison test was used to determine the significance of the correlation compared to F21T + PhenDC3 and F22 conditions, respectively, and values are expressed in mean ± SD and displayed on bars. ****$\rho < 0.0001$.

non-G4 forming samples while values in between correspond to unknown structures), owing to its ability to adopt a stable G4 fold.

3.3. PhpC interaction

Now that the formation of the miR-3196 G4 has been firmly established, it was of interest to investigate its interaction with the molecular helicase PhpC. Fluorescence studies were then conducted to evaluate the interaction between the PhpC and the FAM-rG4–3196 sequence, determining its binding affinity. In this experiment, PhpC was titrated with the pre-annealed FAM-rG4–3196 sequence in IMB buffer, and the FAM fluorescence was monitored. Based on the spectra in Fig. 6, the sequence showed higher fluorescence emission when tested alone. However, upon titration with increasing amounts of PhpC, a decrease in fluorescence was observed. This decrease suggests that the ligand binds to G4, causing fluorescence quenching and indicating a good affinity for G4 RNA. The ligand binding affinity was further analyzed through saturation binding plots derived from maximum fluorescence values and non-linear regression analyses using the two sites – specific binding equation. Two dissociation constants (K_d1 and K_d2) were calculated, yielding values of 15.26 ± 6.29 nM and 4434 ± 1061 nM (mean ± SE), indicating the presence of both high- and low-affinity binding sites. These results confirm the ability of PhpC to recognize and bind to the rG4–3196 sequence.

Additionally, to explore the effect of PhpC on the G4 formation of pre-miR-3196, NMR assays were conducted due to their high atomic resolution at 37 °C. The ^{1}H NMR experiments started with the pre-annealed sequence (100 μM) in K100 to assess the impact of PhpC concentration on the formed G4. At each titration point, PhpC was added directly to the tube, and the sample was annealed as previously described. Detailed analysis of PhpC titration spectra indicated a progressive disruption of G4 with the addition of PhpC (100 to 2000 μM), as evidenced by the loss of Hoogsteen binding signals in the imino region (12.5–9.5 ppm) and the appearance of distinct and more defined signals in the aromatic proton region (9.0–7.0 ppm) (**Fig. S6**). Overall, these findings suggest that PhpC interacts with rG4–3196, disrupting its native

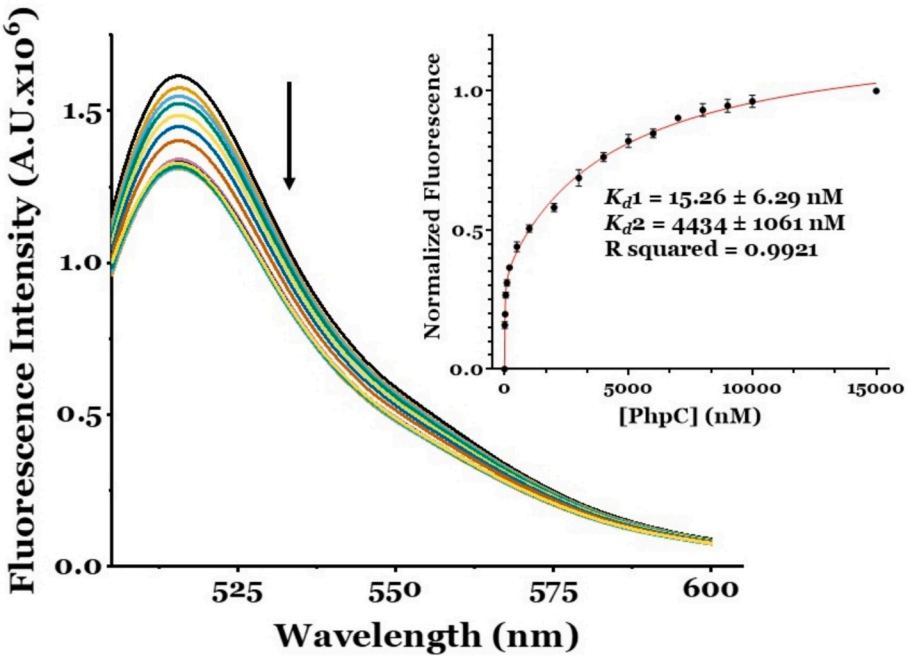

Fig. 6. Interaction between preformed rG4 and PhpC. Fluorescence titrations were performed using the FAM-rG4–3196 sequence with increasing concentrations of the PhpC ligand. The fraction of bound probe was determined and plotted, fitting the data to the saturation binding equation (Michaelis-Menten equation).

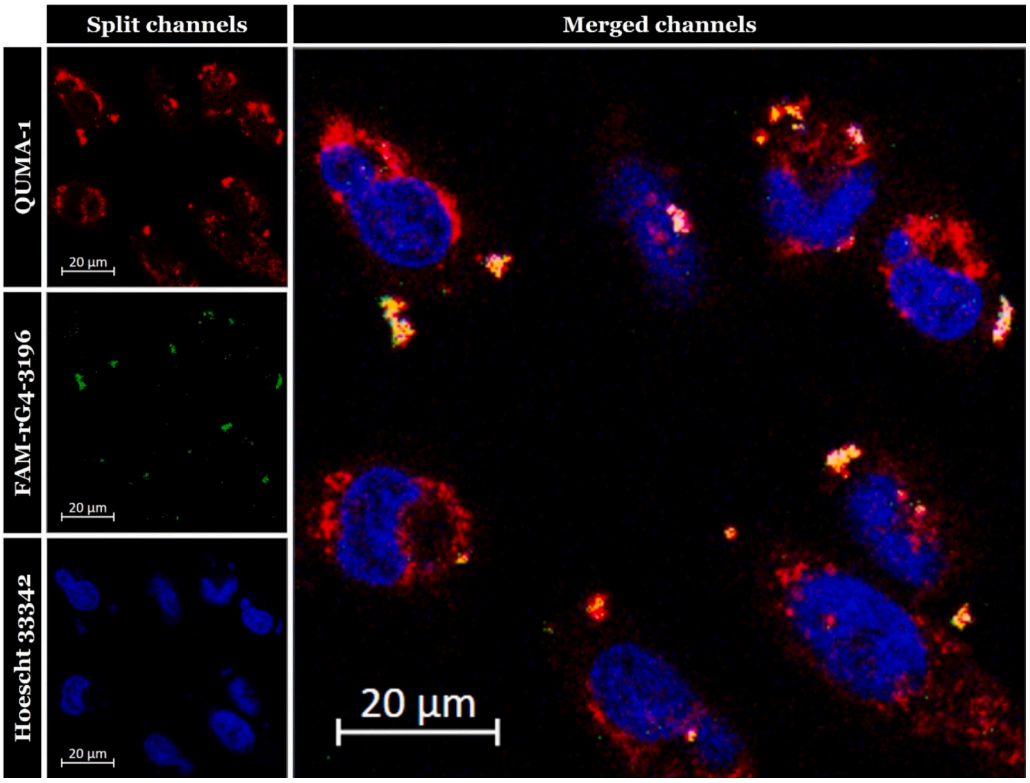

Fig. 7. Live A549 lung cancer cells transfected with 50 nM of FAM-rG4–3196 sequence (in green) and incubated with the QUMA-1 probe (in red) at a concentration of 0.25 µM. Hoechst 33342 (2 µM) was used for nuclear staining (in blue).

G4 conformation and leading to a structural transition.

3.4. In-cell studies of G4 formation

After the demonstration of the existence of a G4 within the rG4–3196 sequence, we aimed to confirm its formation in cells. To this end, A549 LC cells were sequentially treated with a FAM-rG4–3196 sequence (transfected using Lipofectamine), and the RNA G4 marker QUMA-1 [56]. The images obtained (seen in Figs. 7 **and S7**) revealed a strong overlap between the green foci (corresponding to FAM-rG4–3196) and the red foci (corresponding to QUMA-1). This colocalization was quantified through both Manders' overlap coefficient (r) and the

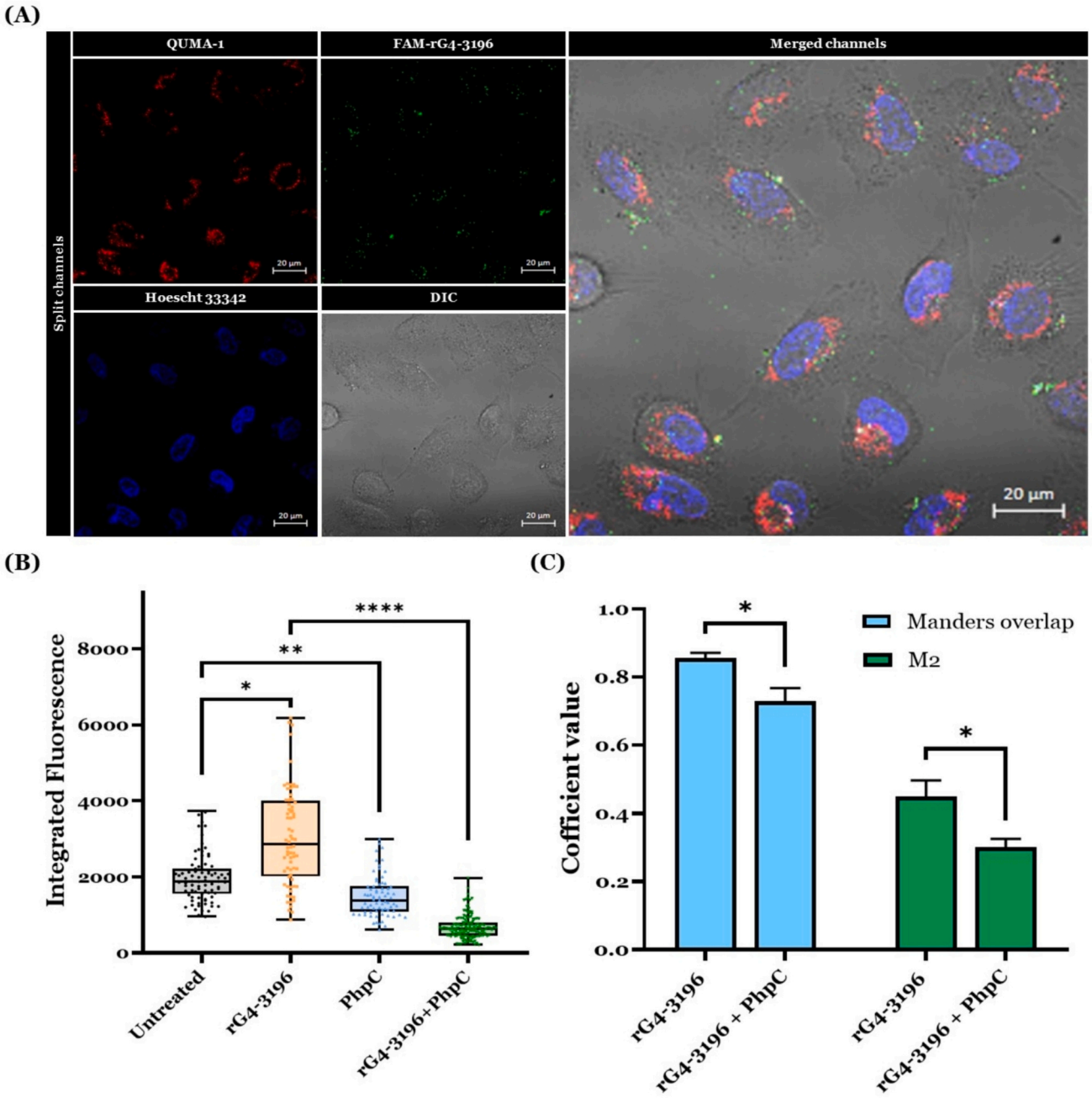

Fig. 8. **(A)** Confocal Scanning Laser Microscopy (CSLM) images of A549 cancer cells transfected with FAM-rG4-3196 (in green) and incubated with PhpC for 24 h. Then, the cells were incubated with a QUMA-1 probe (in red), and Hoechst 33342 was used as a nuclear marker (in blue). **(B)** Integrated fluorescence values *per* cell emitted from the QUMA-1 (red signal) were obtained by employing the software ImageJ in A549 cells without any treatment and after incubation with the PhpC ligand. The Kruskal-Wallis test with Dunn's multiple comparison test was used to determine the significance of the correlations, and values are expressed in mean ± SD. **(C)** Colocalization coefficients were determined using the JACoP plugin with the manual thresholds of 10 and 5 for the FAM-rG4–3196 sequence and the QUMA-1 probe, respectively, with and without PhpC incubation. The two-way ANOVA test with Sidak's multiple comparison test was used to determine the significance of the correlations, and values are expressed in mean ± SD and displayed on bars. *$\rho < 0.05$, **$\rho < 0.01$ and ****$\rho < 0.0001$.

colocalization coefficients M1 and M2 (see **Table S6**): these calculations ($r = 0.81$ and M2 = 0.69) confirmed the high level of colocalization, enabling us to argue that rG4–3196 does form a G4 structure in living A549 cells.

Next, we evaluated whether PhpC was able to modulate rG4–3196 in a cellular environment. To this end, we first performed chemo-fluorescence experiment with QUMA-1 in A549 cells treated or not with PhpC (50 or 100 µM for 24 h, its IC_{50} being ≥100 µM). As seen in **Fig. S8**, the presence of PhpC triggered a 28 % decrease in the G4 landscape as compared to the untreated conditions, which is in line with its G4-unfolding activity (and in line with results obtained in both HeLa and MCF7 cells) [57,58].

Therefore, we performed another series of experiments to study the effect of PhpC on the rG4–3196 in LC cells: A549 cells were transfected with FAM- rG4–3196 sequence (50 nM; 24 h) and then incubated with PhpC (50 µM; 24 h) and the QUMA-1 probe (0.25 µM; 15 min). The images seen in Fig. 8 indicated that the transfection of the rG4–3196 increased the fluorescence signal by 53 %; after incubation of PhpC, the G4 fluorescence signal dropped significantly by 77 %, thus supporting that PhpC likely unfold rG4–3196 in A549 cells. Of note, the

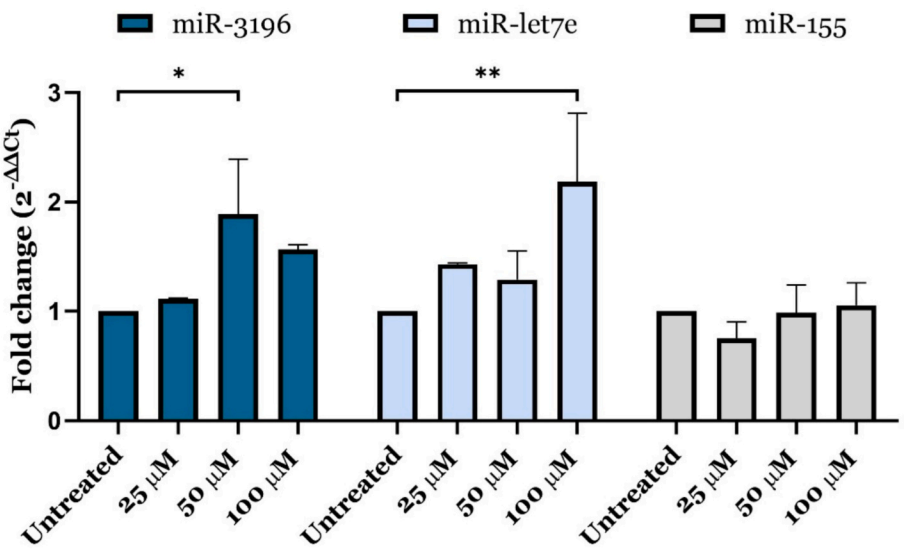

Fig. 9. Levels of miRs transcript after PhpC treatment of A549 cells. RT-qPCR data shows increasing transcript levels of mature miRs (miR-3196, miR-let7e, and miR-155-3p) upon increasing concentration of G4 destabilizing PhpC. The effect of PhpC concentration gradient on cells was compared to the untreated cells. Mature miR levels were normalized by the internal control U6 gene. The two-way ANOVA test with Bonferroni correction was used to determine the significance of the correlation compared to untreated conditions, and values are expressed in mean ± SD and displayed on bars. *$\rho < 0.05$ and **$\rho < 0.01$.

colocalization coefficients (r and M2) were calculated and the decreases observed in both instances (13 % and 15 %) confirmed the G4 disruption by PhpC.

Finally, we aimed to investigate whether the PhpC-mediated unfolding of rG4–3196 in cells has functional consequences. To this end, we assessed the level of mature miR in the absence or presence of PhpC (50 μM; 24 h) by RT-qPCR. As seen in Fig. 9, treatment cells with increasing concentrations of PhpC led to a gradual increase in the transcript level of mature miR-3196 (up 1.9-fold at 50 μM, normalized against the endogenous U6 housekeeping gene) as compared to the untreated conditions. Notably, a slight reduction in fold change was observed at the highest concentration of PhpC. This has already been observed in different experimental setups and might have different origins, first among which is a toggling between G4 destabilization at low doses and secondary interactions (including G4 stabilization) at the highest doses [31]. Also, a possible stress-induced modulation of RNA metabolism cannot be ruled out, which may interfere with miR biogenesis to some extent at this very high concentration. Further investigations are needed to understand the mechanism behind this observation, including a broader analysis of miR processing machinery upon PhpC treatment. As controls, we also assessed the levels of two other miRs, one of them, miR-let7e, having known G4-forming sequences, while miR-155 is known to be devoid of G4-forming sequences. Significantly changes were observed with miR-let7e (up 2.2-fold at 100 μM), while no modifications were monitored with miR-155, indicating that this effect is both G4-dependent and G4-specific.

Altogether, the wealth of *in vitro* and in-cell results shows that rG4–3196 does exist in cells and also can be modulated by PhpC, which effectively enhances the levels of miRs in cells.

4. Conclusion

In this study, our findings reveal the presence of a rG4 structure within the pre-miR-3196 and its pivotal role in the miR biogenesis regulation. This G4 fold was fully characterized by a series of well-established and complementary biophysical methods. This G4, named rG4–3196, was revealed to be highly polymorphic, and able to form multiple species. In A549 living cells, this rG4, when exogenously added, was observed using the RNA G4-specific QUMA probe. Still in cells, we showed here that its folding could be modulated using the molecular helicase PhpC, which quite satisfyingly leads to an increase of miR-3196 levels. These results are unique given that they establish a new strategy to fight against cancer proliferation: indeed, miR-3196 acts as a tumor suppressor through its regulation of oncogenic pathways such as SOX12, FOXP4, and PUMA; we showed that unfolding its G4 allows for enhancing its expression, which in turn could culminate in LC growth suppression.

Overall, these findings emphasize the potential of G4-modulation strategies as a new LC therapeutic approach aiming to restore tumor-suppressive miR expression without the off-target effects commonly associated with small interfering RNAs, synthetic miR mimics, and G4-stabilizing molecules, known to be responsible for severe adverse effects (notably triggering a high level of genetic instability). While our results are encouraging, we are aware of the limitations of our study. For instance, although we showed here that PhpC unfolds the G4 structure in pre-miR-3196, thereby increasing the production of its mature form in cells, we did not investigate the impact of this upregulation on key cancer-related features such as cell growth or death. Also, our study was limited to a single cell line (A549), which does not reflect the complexity of lung cancers. We have also not studied the influence of PhpC on other G4s, which could lead to unintended cellular effects. Finally, as this study is limited to pre-clinical investigations, it is difficult to translate these findings into real-world therapies. Future work should include broader biological experiments, different cell types, and *in vivo* validation to build a stronger case for using PhpC as a targeted therapy.

CRediT authorship contribution statement

Daniela Alexandre: Writing – review & editing, Writing – original draft, Validation, Methodology, Investigation, Formal analysis, Data curation. **Joana Polido:** Writing – review & editing, Methodology, Investigation, Formal analysis, Data curation. **André Miranda:** Writing – review & editing, Methodology, Formal analysis, Data curation. **Robert H.E. Hudson:** Writing – review & editing, Investigation. **David Monchaud:** Writing – review & editing, Formal analysis, Data curation. **Pedro V. Baptista:** Writing – review & editing, Supervision, Project administration, Methodology, Investigation, Formal analysis, Data curation. **Carla Cruz:** Writing – review & editing, Validation, Supervision, Project administration, Methodology, Investigation, Funding acquisition, Formal analysis, Data curation, Conceptualization.

Funding

Daniela Alexandre and André Miranda acknowledge the doctoral fellowship grants from FCT – Foundation for Science and Technology ref. 2021.07695.BD and 2021.04785.BD, respectively. Thanks are due to CICS-UBI program funding DOI 10.54499/UIDB/00709/2020 (https://doi.org/10.54499/UIDB/00709/2020) and the CICS-UBI program funding with DOI 10.54499/UIDP/00709/2020 (https://doi.org/10.54499/UIDP/00709/2020) with national funds from the Foundation for Science and Technology, PPBI-Portuguese Platform of BioImaging research unit (POCI-01-0145-FEDER-022122), and to the Portuguese NMR Network (ROTEIRO/0031/2013-PINFRA/22161/2016), through national funds and, where applicable, co-financed by the FEDER through COMPETE 2020, POCI, PORL and PIDDAC. C.C. acknowledges the grants from project PAPILOMA ref. CENTRO-01-0145-FEDER-181235, NRC-LPCC Bolsa Dr. Rocha Alves 2022, Instruct-ERIC Pilot R&D application ID 2473. This work was supported by EATRIS, the European infrastructure for translational medicine.

Declaration of competing interest

The authors declare that they have no known competing financial interests or personal relationships that could have appeared to influence the work reported in this paper.

Acknowledgments

None.

Appendix A. Supplementary Data

Supplementary Data are available online and include a list of oligonucleotides and ligands used in the experiments, CD spectra, melting temperature in different buffers acquired by CD-melting, TDS and IDS data, colocalization coefficients, ^{1}H NMR spectra of rG4 pre-miR-3196 after addition of KCl and PhpC, polyacrylamide gel electrophoresis with NMM or SYBR Gold staining, SEC chromatography results and fluorescence confocal microscopy images in A549 cell line of transfected FAM-rG4–3196 sequence and PhpC ligand.Supplementary data to this article can be found online at https://doi.org/10.1016/j.ijbiomac.2025.145263.

Data availability

No data was used for the research described in the article.

References

[1] S. Takahashi, N. Sugimoto, Stability prediction of canonical and non-canonical structures of nucleic acids in various molecular environments and cells, Chem. Soc. Rev. 49 (2020) 8439–8468, https://doi.org/10.1039/d0cs00594k.
[2] J. Jana, S. Mohr, Y.M. Vianney, K. Weisz, Structural motifs and intramolecular interactions in non-canonical G-Quadruplexes, RSC Chem Biol 2 (2021) 338–353, https://doi.org/10.1039/d0cb00211a.
[3] A.N. Lacen, A. Symasek, A. Gunter, H.T. Lee, Slow G-Quadruplex conformation rearrangement and accessibility change induced by potassium in human Telomeric single-stranded DNA, J. Phys. Chem. B 128 (2024) 5950–5965, https://doi.org/10.1021/acs.jpcb.4c00719.
[4] J. Spiegel, S. Adhikari, S. Balasubramanian, The structure and function of DNA G-Quadruplexes, Trends Chem. 2 (2020) 123–136, https://doi.org/10.1016/j.trechm.2019.07.002.
[5] K. Lyu, E.Y.C. Chow, X. Mou, T.F. Chan, C.K. Kwok, RNA G-Quadruplexes (RG4s): genomics and biological functions, Nucleic Acids Res. 49 (2021) 5426–5450, https://doi.org/10.1093/nar/gkab187.
[6] L.R. Ganser, M.L. Kelly, D. Herschlag, H.M. Al-Hashimi, The Roles of Structural Dynamics in the Cellular Functions of RNAs, Nat. Rev. Mol. Cell Biol. 20 (2019) 474–489, https://doi.org/10.1038/s41580-019-0136-0.
[7] A. Vannutelli, S. Belhamiti, J.M. Garant, A. Ouangraoua, J.P. Perreault, Where are G-Quadruplexes located in the human transcriptome? NAR Genom Bioinform 2 (2020) https://doi.org/10.1093/nargab/lqaa035.
[8] Leïla Dumas, Pauline Herviou, Erik Dassi, Anne Cammas, Stefania Millevoi, G-Quadruplexes, RNA Biology, Recent Advances and Future Directions 46 (2021) 270–283, https://doi.org/10.1016/j.tibs.2020.11.001.
[9] K. Lyu, E.Y.C. Chow, X. Mou, T.F. Chan, C.K. Kwok, RNA G-Quadruplexes (RG4s): genomics and biological functions, Nucleic Acids Res. 49 (2021) 5426–5450, https://doi.org/10.1093/nar/gkab187.
[10] M. Tassinari, S.N. Richter, P. Gandellini, Biological relevance and therapeutic potential of G-Quadruplex structures in the human noncoding transcriptome, Nucleic Acids Res. 49 (2021) 3617–3633, https://doi.org/10.1093/nar/gkab127.
[11] N. Kosiol, S. Juranek, P. Brossart, A. Heine, K. Paeschke, G-Quadruplexes: a promising target for Cancer therapy, Mol. Cancer 20 (2021) 1–18, https://doi.org/10.1186/s12943-021-01328-4.
[12] S.K. Ganegamage, M.D. Heagy, Illuminating the G-Quadruplex: a review on fluorescent probes for detecting G-quartet DNA structures, Curr. Org. Chem. 26 (2022) 1004–1054, https://doi.org/10.2174/1385272826666220811102939.
[13] D. Varshney, J. Spiegel, K. Zyner, D. Tannahill, S. Balasubramanian, The regulation and functions of DNA and RNA G-Quadruplexes Europe PMC funders group, Nat. Rev. Mol. Cell Biol. 21 (2020) 459–474, https://doi.org/10.1038/s41580-020-0236-x.
[14] K.G. Zyner, D.S. Mulhearn, S. Adhikari, S.M. Cuesta, M. Di Antonio, N. Erard, G. J. Hannon, D. Tannahill, S. Balasubramanian, Genetic interactions of G-Quadruplexes in humans, Elife 8 (2019) e46793, https://doi.org/10.7554/elife.46793.
[15] J. Cable, E. Heard, T. Hirose, K.V. Prasanth, L.L. Chen, J.E. Henninger, S. A. Quinodoz, D.L. Spector, S.D. Diermeier, A.M. Porman, et al., Noncoding RNAs: biology and applications—a keystone Symposia report, Ann. N. Y. Acad. Sci. 1506 (2021) 118–141, https://doi.org/10.1111/nyas.14713.
[16] Y. Peng, C.M. Croce, The Role of MicroRNAs in Human Cancer, Sig. Transduct. Target Ther. 1 (2016) 15004, https://doi.org/10.1038/sigtrans.2015.4.
[17] L.-A. MacFarlane, R. Murphy, P., MicroRNA: biogenesis, function and role in Cancer, Curr. Genomics 11 (2010) 537–561, https://doi.org/10.2174/138920210793175895.
[18] P. Naeli, T. Winter, A.P. Hackett, L. Alboushi, S.M. Jafarnejad, The intricate balance between MicroRNA-induced MRNA decay and translational repression, FEBS J. 290 (2023) 2508–2524, https://doi.org/10.1111/FEBS.16422.
[19] J.A. Imperatore, M.L. Then, K.B. McDougal, M.R. Mihailescu, Characterization of a G-Quadruplex structure in pre-MiRNA-1229 and in its Alzheimer's disease-associated variant Rs2291418: implications for MiRNA-1229 maturation, Int. J. Mol. Sci. 21 (2020) 767, https://doi.org/10.3390/IJMS21030767.
[20] G. Mirihana Arachchilage, A.C. Dassanayake, S. Basu, A potassium ion-dependent RNA structural switch regulates human pre-MiRNA 92b maturation, Chem. Biol. 22 (2015) 262–272, https://doi.org/10.1016/j.chembiol.2014.12.013.
[21] S. Pandey, P. Agarwala, G.G. Jayaraj, R. Gargallo, S. Maiti, The RNA stem-loop to G-Quadruplex equilibrium controls mature MicroRNA production inside the cell, Biochemistry 54 (2015) 7067–7078, https://doi.org/10.1021/acs.biochem.5b00574.
[22] G. Liu, W. Du, H. Xu, Q. Sun, D. Tang, S. Zou, Y. Zhang, M. Ma, G. Zhang, X. Du, et al., RNA G-Quadruplex regulates MicroRNA-26a biogenesis and function, J. Hepatol. 73 (2020) 371–382, https://doi.org/10.1016/j.jhep.2020.02.032.
[23] O.S. Vinchure, K. Whittemore, D. Kushwah, M.A. Blasco, R. Kulshreshtha, MiR-490 suppresses telomere maintenance program and associated hallmarks in glioblastoma, Cell. Mol. Life Sci. 78 (2021) 2299–2314, https://doi.org/10.1007/S00018-020-03644-2.
[24] J.A. Imperatore, M.L. Then, K.B. McDougal, M.R. Mihailescu, Characterization of a G-Quadruplex Structure in Pre-MiRNA-1229 and in Its Alzheimer's Disease-Associated Variant Rs2291418: Implications for MiRNA-1229 Maturation, Int. J. Mol. Sci. 21 (2020) 767, https://doi.org/10.3390/ijms21030767.
[25] G. Mirihana Arachchilage, P. Kharel, J. Reid, S. Basu, Targeting of G-Quadruplex harboring pre-MiRNA 92b by LNA rescues PTEN expression in NSCL Cancer cells, ACS Chem. Biol. 13 (2018) 909–914, https://doi.org/10.1021/acschembio.7b00749.
[26] J. Figueiredo, J.L. Mergny, C. Cruz, G-Quadruplex ligands in Cancer therapy: Progress, challenges, and clinical perspectives, Life Sci. 340 (2024) 122481, https://doi.org/10.1016/j.lfs.2024.122481.
[27] J. Figueiredo, T. Santos, A. Miranda, D. Alexandre, B. Teixeira, P. Simões, J. Lopes-Nunes, C. Cruz, Ligands as Stabilizers of G-Quadruplexes in Non-Coding RNAs, Molecules 26 (2021) 6164, https://doi.org/10.3390/molecules26206164.
[28] J.F. Moruno-Manchon, P. Lejault, Y. Wang, B. McCauley, P. Honarpisheh, D.A. M. Scheihing, S. Singh, W. Dang, N. Kim, A. Urayama, et al., Small-Molecule G-Quadruplex Stabilizers Reveal a Novel Pathway of Autophagy Regulation in Neurons, Elife 9 (2020), https://doi.org/10.7554/ELIFE.52283.
[29] N. Tabor, C. Ngwa, J. Mitteaux, M.D. Meyer, J.F. Moruno-Manchon, L. Zhu, F. Liu, D. Monchaud, L.D. McCullough, A.S. Tsvetkov, Differential Responses of Neurons, Astrocytes, and Microglia to G-Quadruplex Stabilization, Aging 13 (2021) 15917–15941, https://doi.org/10.18632/AGING.203222.
[30] G. Fracchioni, S. Vailati, M. Grazioli, V. Pirota, Structural Unfolding of G-Quadruplexes: From Small Molecules to Antisense Strategies, Molecules 29 (2024) 3488, https://doi.org/10.3390/molecules29153488.
[31] J. Mitteaux, P. Lejault, F. Wojciechowski, A. Joubert, J. Boudon, N. Desbois, C. P. Gros, R.H.E. Hudson, J.B. Boulé, A. Granzhan, et al., Identifying G-Quadruplex-DNA-disrupting small molecules, J. Am. Chem. Soc. 143 (2021) 12567–12577, https://doi.org/10.1021/jacs.1c04426.
[32] Y. Ma, X. Pan, P. Xu, Y. Mi, W. Wang, X. Wu, Q. He, X. Liu, W. Tang, H.X. An, Plasma MicroRNA alterations between EGFR-activating mutational NSCLC patients with and without primary resistance to TKI, Oncotarget 8 (2017) 88529, https://doi.org/10.18632/oncotarget.19874.

[33] C. Xu, L. Zhang, L. Duan, C. Lu, MicroRNA-3196 is inhibited by H2AX phosphorylation and attenuates lung Cancer cell apoptosis by downregulating PUMA, Oncotarget 7 (2016) 77764, https://doi.org/10.18632/oncotarget.12794.
[34] W. Qi, C. Gao, L. Zhang, Z. Gao, J. Sui, C. Han, D. Sun, MiR-3196, a P53-responsive MicroRNA, functions as a tumor suppressor in hepatocellular carcinoma by targeting FOXP4, Am. J. Cancer Res. 9 (2019) 2665–2678. PMID: 31911853.
[35] Q. Wu, J. Jiang, LncRNA MAFG-AS1 promotes lung adenocarcinoma cell migration and invasion by targeting MiR-3196 and regulating SOX12 expression, Mol. Biotechnol. 64 (2022) 970–983, https://doi.org/10.1007/s12033-022-00455-7.
[36] R. Lorenz, S.H. Bernhart, C. Höner zu Siederdissen, H. Tafer, C. Flamm, P. F. Stadler, I.L. Hofacker, ViennaRNA Package 2.0, Algorithms Mol. Biol. 6 (2011), https://doi.org/10.1186/1748-7188-6-26.
[37] A. Kozomara, M. Birgaoanu, S. Griffiths-Jones, MiRBase: from MicroRNA sequences to function, Nucleic Acids Res. 47 (2019) 155–162, https://doi.org/10.1093/nar/gky1141.
[38] A. Bedrat, L. Lacroix, J.L. Mergny, Re-evaluation of G-Quadruplex propensity with G4Hunter, Nucleic Acids Res. 44 (2016) 1746–1759, https://doi.org/10.1093/nar/gkw006.
[39] J. Chen, M. Cheng, P. Stadlbauer, J. Šponer, J.L. Mergny, H. Ju, J. Zhou, Exploring sequence space to design controllable G-Quadruplex topology switches, CCS Chemistry 41 (2022) 3036–3050, https://doi.org/10.31635/ccschem.021.202101357.
[40] J.L. Mergny, J. Li, L. Lacroix, S. Amrane, J.B. Chaires, Thermal difference spectra: a specific signature for nucleic acid structures, Nucleic Acids Res. 33 (2005) e138, https://doi.org/10.1093/nar/gni134.
[41] A. Miranda, T. Santos, E. Largy, C. Cruz, Locking up the AS1411 aptamer with a flanking duplex: towards an improved Nucleolin-targeting, Pharmaceuticals (Basel) 14 (2021) 1–20, https://doi.org/10.3390/ph14020121.
[42] M. Deiana, M. Mosser, T. Le Bahers, E. Dumont, M. Dudek, S. Denis-Quanquin, N. Sabouri, C. Andraud, K. Matczyszyn, C. Monnereau, et al., Light-induced in situ chemical activation of a fluorescent probe for monitoring intracellular G-Quadruplex structures, Nanoscale 13 (2021) 13795–13808, https://doi.org/10.1039/d1nr02855c.
[43] T. Santos, A. Miranda, L. Imbert, A. Jardim, C.R.F. Caneira, V. Chu, J.P. Conde, M. P.C. Campello, A. Paulo, G. Salgado, et al., Pre-MiRNA-149 G-Quadruplex as a Molecular Agent to Capture Nucleolin, Eur. J. Pharm. Sci. 169 (2022) 106093, https://doi.org/10.1016/j.ejps.2021.106093.
[44] E. Largy, J.-L. Mergny, Shape matters: size-exclusion HPLC for the study of nucleic acid structural polymorphism, Nucleic Acids Res. 42 (2014), https://doi.org/10.1093/nar/gku751.
[45] A. Miranda, A. Cucchiarini, C. Esnault, J.C. Andrau, P.A. Oliveira, J.L. Mergny, C. Cruz, G-Quadruplex forming motifs in the promoter region of the B-MYB proto-oncogene, Int. J. Biol. Macromol. 270 (2024) 132244, https://doi.org/10.1016/j.ijbiomac.2024.132244.
[46] Y. Luo, A. Granzhan, D. Verga, J.L. Mergny, FRET-MC: a fluorescence melting competition assay for studying G4 structures in vitro, Biopolymers 112 (2021) e23415, https://doi.org/10.1002/bip.23415.
[47] Y. Luo, D. Verga, J.L. Mergny, Iso-FRET: An isothermal competition assay to analyze Quadruplex formation in vitro, Nucleic Acids Res. 50 (2022) e93, https://doi.org/10.1093/nar/gkac465.
[48] J.E. Park, I. Heo, Y. Tian, D.K. Simanshu, H. Chang, D. Jee, D.J. Patel, V.N. Kim, Dicer recognizes the 5′ end of RNA for efficient and accurate processing, Nature 475 (2011) 201–205, https://doi.org/10.1038/nature10198.
[49] J. Dickerhoff, J. Jang, D. Yang, Best method to determine DNA G-Quadruplex folding: the 1H–13C HSQC NMR experiment, Methods 221 (2024) 35–41, https://doi.org/10.1016/j.ymeth.2023.11.013.
[50] M. Adrian, B. Heddi, A.T. Phan, NMR Spectroscopy of G-Quadruplexes. *Methods* 57 (2012) 11–24, https://doi.org/10.1016/j.ymeth.2012.05.003.
[51] C. Hennecker, L. Yamout, C. Zhang, C. Zhao, D. Hiraki, N. Moitessier, A. Mittermaier, Structural polymorphism of guanine Quadruplex-containing regions in human promoters, Int. J. Mol. Sci. 23 (2022) 16020, https://doi.org/10.3390/ijms232416020/s1.
[52] N.C. Sabharwal, V. Savikhin, J.R. Turek-Herman, J.M. Nicoludis, V.A. Szalai, L. A. Yatsunyk, N-Methylmesoporphyrin IX fluorescence as a reporter of Strand orientation in guanine Quadruplexes, FEBS J. 281 (2014) 1726–1737, https://doi.org/10.1111/febs.12734.
[53] A.R. De La Faverie, A. Guédin, A. Bedrat, L.A. Yatsunyk, J.L. Mergny, Thioflavin T as a fluorescence light-up probe for G4 formation, Nucleic Acids Res. 42 (2014), https://doi.org/10.1093/nar/gku111.
[54] A. De Cian, E. DeLemos, J.L. Mergny, M.P. Teulade-Fichou, D. Monchaud, Highly efficient G-Quadruplex recognition by Bisquinolinium compounds, J. Am. Chem. Soc. 129 (2007) 1856–1857, https://doi.org/10.1021/ja067352b.
[55] Y. Luo, A. Granzhan, D. Verga, J.L. Mergny, FRET-MC: a fluorescence melting competition assay for studying G4 structures in vitro, Biopolymers 112 (2021) e23415, https://doi.org/10.1002/bip.23415.
[56] X.C. Chen, S.Bin Chen, J. Dai, J.H. Yuan, T.M. Ou, Z.S. Huang, J.H. Tan, Tracking the dynamic folding and unfolding of RNA G-Quadruplexes in live cells, Angew. Chem. Int. Ed. 57 (2018) 4702–4706, https://doi.org/10.1002/anie.201801999/full.
[57] A. De Magis, M. Limmer, V. Mudiyam, D. Monchaud, S. Juranek, K. Paeschke, UV-induced G4 DNA structures recruit ZRF1 which prevents UV-induced senescence, Nat. Commun. 14 (2023) 1–16, https://doi.org/10.1038/s41467-023-42494-x.
[58] J. Mitteaux, S. Raevens, Z. Wang, M. Pirrotta, I.E. Valverde, R.H.E. Hudson, D. Monchaud, PhpC modulates G-Quadruplex-RNA landscapes in human cells, Chem. Commun. 60 (2024) 424–427, https://doi.org/10.1039/d3cc05155b.
[59] V.K. Vijay, J. Mitteaux, Z. Wang, E. Wheeler, N. Tandon, S. Yun Jung, R.H. E. Hudson, D. Monchaud, A.S. Tsvetkov, Small Molecule-Based Regulation of Gene Expression in Human Astrocytes Switching on and off the G-Quadruplex Control Systems, J. Biol. Chem. 301 (2025) 108040, https://doi.org/10.1016/J.JBC.2024.108040.